Journal of Zhejiang University-SCIENCE A (Applied Physics & Engineering)
ISSN 1673-565X (Print); ISSN 1862-1775 (Online)
www.jzus.zju.edu.cn; www.springerlink.com
E-mail: jzus@zju.edu.cn

Scale-resolving simulation and particle image velocimetry validation of the flow around a marine propeller*

Chun-bao LIU[1,2], Jing LI[1], Yuan LI[1], Tong-jian WANG[†‡1]

[1]*School of Mechanical and Aerospace Engineering, Jilin University, Changchun 130022, China*

[2]*State Key Laboratory of Automotive Simulation and Control, Jilin University, Changchun 130022, China*

[†]E-mail: wangtj@jlu.edu.cn

Received Apr. 23, 2019; Revision accepted July 20, 2019; Crosschecked July 23, 2019

Abstract: There are many unresolved issues in Reynolds-averaged Navier-Stokes (RANS) calculations of marine propeller performance, especially in the treatment of complex flow phenomena such as boundary-layer development, scale effects, and tip and hub vortices. The particular focus of this study was to apply three scale-resolving simulation (SRS) methods, i.e. dynamic large eddy simulation (DLES), delayed detached-eddy simulation (DDES), and stress-blended eddy simulation (SBES), to improve the prediction of flow characteristics. Firstly, the effectiveness of the SRS methods was verified by comparing numerical results with experimental data. The external performance of rotating machinery is determined by internal flow structures. Particle image velocimetry (PIV) measurement is established as a visualization tool to analyze the wake evolution of a scaled propeller by velocity and vorticity contours in a specified cross-section plane. We found that SRS methods, especially the SBES model, performed well in predicting characteristic parameters and capturing flow field information via quantitative and qualitative analyses. The ability to accurately predict flow characteristics can make computational tools more effective in meeting the needs of modern propeller design and analysis.

Key words: Propeller; Numerical simulation; Scale-resolving simulation (SRS); Particle image velocimetry (PIV) test
https://doi.org/10.1631/jzus.A1900165 **CLC number:** TB126

1 Introduction

In a flow field, turbulence is a typical flow phenomenon in the fluid of machinery, such as pumps, turbines, wind turbines, and propellers. Turbulence is an irregular, structured, multi-scale, and complex unsteady flow with extremely strong dissipation and diffusivity (Yang, 2015). Since its invention, the marine propeller has played a vital role in the shipbuilding industry as a widely used thruster. Compared to conventional pumps and turbines, a marine propeller has geometric characteristics of variable blade section, chord length, and pitch angle. It is critically important to accurately simulate the wake flow in the design and performance analysis of a marine propulsion system. To design a propeller to meet heavy load and high speed requirements, the integration of computational fluid dynamics (CFD) and experimental techniques could be a useful approach.

Many calculations of the turbulent flow around propellers have been conducted with various codes and turbulence models, such as Reynolds-averaged Navier-Stokes (RANS) (Morgut and Nobile, 2012; Yao, 2015; Mizzi et al., 2017), large eddy simulation

‡ Corresponding author

* Project supported by the Key Scientific and Technological Project of Jilin Province (No. 20170204066GX), the Science and Technology Projects in Department of Education, Jilin Province (No. JJKH20170785KJ), and the Advanced Manufacturing Projects of Government and University Co-construction Program Funded by Jilin Province (No. SXGJSF2017-2), China

ORCID: Chun-bao LIU, https://orcid.org/0000-0002-8265-2875

(LES) (Kumar and Mahesh, 2015, 2016, 2017; Dubbioso et al., 2017), and detached eddy simulation (DES) (Chase and Carrica, 2013; Mofidi and Carrica, 2014). Most calculations have achieved reasonable consistency in predicting the overall performance and flow characteristics of propellers. However, some difficult issues, including intensive vortex interaction, reduction of accuracy prediction under heavy load and high speed conditions, still need to be addressed. In addition, experimental measurement or numerical study based on the latest advanced stress-blended eddy simulation (SBES) of scale-resolving simulation (SRS) solver to investigate the characteristics of wake is very rare. There is also a lack of relevant publications listing in detail the visualization features of the CFD method in propeller performance prediction.

Numerical simulation can shorten the design cycle and provide detailed flow field information for fluid dynamics. However, the accuracy of numerical simulation needs to be verified by physical test results. Therefore, a fluid testing device is indispensable from the viewpoint of analyzing the internal flow mechanism. In recent years, researchers have increasingly used particle image velocimetry (PIV) tests to measure and analyze velocity information of a propeller wake, because of their ability to measure a wide area in a relatively short time (Ning and Hu, 2016; Ning et al., 2017; Yang et al., 2018). Seo et al. (2016) used a 2D-PIV system to measure the mean velocity and turbulence properties of the downstream flow field of a KVLCC2 propeller model in a towing tank, and reconstructed the 3D flow field. The results were compared with those from other tests to validate their accuracy. Felli et al. (2015) used tomographic PIV to analyze the complex mechanism of a hub vortex and vortex pairing that formed intertwined filaments, including the tip vortex and the secondary weak vortex generated at the leading edge of the blades. They revealed that the radiated noise of the marine propeller emanated mainly from the tip vortex. Yang et al. (2017) used PIV measurements to analyze the interaction between the wing-tip eddy and the propeller, and to quantify the velocity of the vortex upstream and downstream from the propeller.

Many researchers have carried out propeller numerical simulations while conducting PIV tests, and have studied the distribution of the flow field information by comparing the results (Kleinwächter et al., 2015, 2017). Paik et al. (2015) used RANS numerical simulation and stereoscopic PIV to study the wake characteristics of a counter-rotating propeller. In the cases of no propeller, a single propeller at the bow, and two propellers at the bow and stern, the propeller operation was validated by comparing the simulation results with the rudder leading edge test. Korsström et al. (2015) not only introduced a scaled propeller model in PIV measurement, but also used boundary element method (BEM), unsteady Reynolds-averaged Navier–Stokes (URANS) and shear-stress transport (SST) models in numerical simulation. Nevertheless, the applications of SRS methods were still seldom mentioned.

In the following, brief descriptions of SRS models are provided in Section 2. The mesh generation and predicted velocity components of an entire propeller are presented in Section 3. The setup and introduction of PIV measurements are described in Section 4. The results of a flow field analysis of a 1/5 scale propeller experiment are compared with those from CFD in Section 5. Finally, a summary and concluding remarks are included in Section 6.

2 Numerical method

Scale-resolving simulation includes mainly LES and the hybrid RANS-LES simulation (HRL) (Liu et al., 2018). Delay detached eddy simulation (DDES) is a hybrid RANS-LES mode used to effectively reduce the grid dependence of the DES method. In this formulation, the wall boundary layers are completely computed in the RANS model and the free shear flows away from walls are typically covered by the LES mode. An empirical delay function is used, which equals 1 in the boundary layer and falls to 0 rapidly at the edge of the boundary layer. This protects the RANS region from being prematurely switched to a LES region by optimizing the turbulence characteristic length.

The calculation efficiency of DDES is higher than that of LES, but lower than that of RANS. However, when DDES solves the turbulence problem with large geometric buckling of the wall boundary surface, the grid induced separation phenomenon still occurs, which leads to premature conversion to the LES method to solve the near wall region. This leads to increased errors in the captured information, which

hinders the whole development of movement of the turbulence structures. Based on the DDES model, some researchers have proposed a more advanced SBES model. The advantages of this method are as follows: (I) it introduces a blending function to effectively prevent the grid induced separation phenomenon, provide protection against the RANS model of the wall boundary layer region, and make the flow field structures solved by RANS and LES clearer and more visual; (II) it provides a clear conversion between LES and RANS models, and improves grid scale recognition enabling a faster switch between RANS and LES models; (III) it selects any sub-grid model to combine with the RANS model more flexibly. The characteristics of the three scale-resolving simulations are shown in Table 1.

In Table 1, L_{ij} is the second-order tensor, T_{ij} is the test-filtered subgrid scale stress tensor, τ_{ij} is the subgrid scale stress tensor, u_i and u_j are the velocity components, C_{DSL} and C_{SBES} are the model coefficients, ρ is the fluid density, Δ is the filter width, S is the strain rate, S_{ij} is the resolved strain rate tensor, M_{ij} is the generalized tensor, δ_{ij} is the Kronecker delta, l_{RANS}, l_{LES}, and l_{DDES} are the turbulent length scales, f_{DDES} and f_{SBES} are the shielding functions, r_{d} is the ratio of a model length scale to the wall distance, ν is the molecular viscosity, ν_{t} is the kinematic eddy viscosity, $U_{i,j}$ is the velocity gradients, κ is the Karman constant, d is the distance to the wall, $\varepsilon_{\mathrm{SBES}}$ is the additional sink term, β^* is a coefficient, F_{SBES} is the blending function, k is the turbulent kinetic energy, ω is the turbulent dissipation rate, and Δ_{SBES} is the mesh length scale used in SBES, μ_{t} is the turbulent viscosity, and $\tau_{ij}^{\mathrm{SBES}}$, τ_{ij}^{SST}, τ_{ij}^{DSL} are the viscous stress tensors. Besides, the symbols "–", "^" and "~" denote time-averaged quantities, filtering terms, and Favre-averaged quantities, respectively.

3 Scale-resolving simulation of the entire propeller

3.1 Mesh layout and simulation details

The marine-propeller (P5168) used in this study was designed by Chesnakas and Jessup (1998) at the David Taylor Model Basin. It is a representative

Table 1 Characteristics of different scale-resolving simulations

Model	Mathematical mechanism	Solving ideas	Calculating quantities	Application
DLES (Jahoda et al., 2007; Li et al., 2013)	$L_{ij}=T_{ij}-\hat{\tau}_{ij}=\overline{\tilde{u}_i\tilde{u}_j}-\hat{\tilde{u}}_i\hat{\tilde{u}}_j$, $\tau_{ij}=-2C_{\mathrm{DSL}}\bar{\rho}\Delta^2\lvert\tilde{S}\rvert\left(\tilde{S}_{ij}-\frac{1}{3}\tilde{S}_{kk}\delta_{ij}\right)$, $T_{ij}=-2C_{\mathrm{DSL}}\hat{\bar{\rho}}\hat{\Delta}^2\lvert\hat{\tilde{S}}\rvert\left(\hat{\tilde{S}}_{ij}-\frac{1}{3}\hat{\tilde{S}}_{kk}\delta_{ij}\right)$, $C_{\mathrm{DSL}}M_{ij}=L_{ij}-\frac{1}{3}L_{kk}\delta_{ij}$, $M_{ij}=-2\hat{\Delta}^2\hat{\bar{\rho}}\lvert\hat{\tilde{S}}\rvert\hat{\tilde{S}}_{ij}+2\Delta^2\bar{\rho}\lvert\tilde{S}\rvert\tilde{S}_{ij}$	Solve the larger eddy directly, and treat the smaller eddy with the dynamic Smagorinsky-Lilly subgrid model	More	Many more
DDES (Gritskevich et al., 2012; Lin et al., 2018)	$l_{\mathrm{DDES}}=l_{\mathrm{t}}-f_{\mathrm{DDES}}\cdot\max\{0, l_{\mathrm{t}}-l_{\mathrm{LES}}\}$, $f_{\mathrm{DDES}}=1-\tanh[(8r_{\mathrm{d}})^3]$, $r_{\mathrm{d}}\equiv\frac{\nu_{\mathrm{t}}+\nu}{\sqrt{U_{i,j}U_{i,j}}\kappa^2d^2}$	Convert between LES and RANS algorithms based on the grid precision	Less	More
SBES (Menter, 2012)	$\varepsilon_{\mathrm{SBES}}=-\beta^*\rho k\omega F_{\mathrm{SBES}}$, $F_{\mathrm{SBES}}=\left[\max\left(\frac{L_{\mathrm{t}}}{C_{\mathrm{SBES}}\Delta_{\mathrm{SBES}}}(1-f_{\mathrm{SBES}}),1\right)-1\right]$, $f_{\mathrm{SBES}}=[\exp(y^+/6-45)+1]^{-3/25}$, $\mu_{\mathrm{t}}=(0.2862C_{\mathrm{DSL}}\Delta)^2S$, $\tau_{ij}^{\mathrm{SBES}}=f_{\mathrm{SBES}}\tau_{ij}^{\mathrm{SST}}+(1-f_{\mathrm{SBES}})\tau_{ij}^{\mathrm{DSL}}$	Convert between LES and RANS algorithms based on the grid precision; introduce a hybrid function to protect RANS mode of the wall boundary layer region	Fewer	Much fewer

DLES: dynamic large eddy simulation

five-blade controllable-pitch propeller with a diameter of D=402.7 mm, and provides detailed velocity field measurements. The fixed field was defined as a cylinder with a diameter of 5D and a length of 20D. Due to skewed propeller blades, the rotating field was also set as a cylinder that had a diameter of 1.2D and a length of 1.72D. A grid interface was set up to connect the two fields so that these two grids could slide relatively. Considering the periodic layout of blades and the calculation consumption, 1/5 part was extracted to conduct the study (Fig. 1a). To improve capture of the flow information, especially from the viscous sublayer, a local-grid refinement method was applied to obtain sufficient resolution near the blades. The cell height of the first layer grid was about 0.001D, and the stretching ratio of the layers was 1.1–1.2. The distribution of y^+ on the blade surface (Fig. 1b) ensured proper viscous sublayer resolution. Finally, the total number of grids was 5.2 million, of which 2.2 million were in the rotating field and 3.0 million were in the fixed field. Among them, the maximum volume of the grid was 5 mm^3 and the minimum was 0.2 mm^3. The multiple reference frame (MRF) method was used to transmit the flow information between the two fields. ANSYS FLUENT software was employed to solve the Navier-Stokes equations. The detailed properties of the numerical simulation are summarized in Table 2.

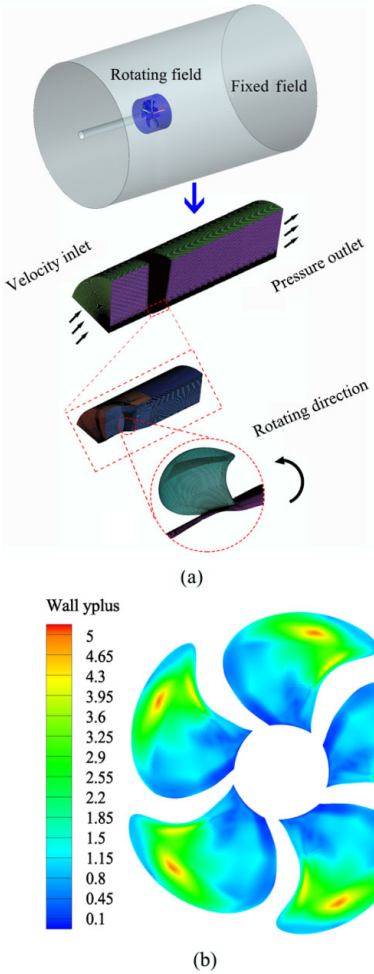

Fig. 1 Numerical simulation model of the entire propeller
(a) Calculation domain and grid layout; (b) Distribution of y^+ at the blade surface

Table 2 CFD model description

Analysis type	Transient state
Pressure-velocity coupling	Semi-implicit method for pressure-linked equations consistent (SIMPLEC)
Momentum	Bounded central differencing
Transient formulation	Second-order implicit
Inlet	Velocity-inlet with 1% turbulence intensity
Outlet	Pressure-outlet with 0 static pressure
Viscosity (Pa·s)	1.003×10^{-3}
Density (kg/m^3)	998.2
Time step size (ms)	0.5
Number of time steps	1000

3.2 Numerical simulation results

The numerical predictions were under the operating condition that the advance coefficient (J) was 1.1, with a free stream velocity of 8.86 m/s and a revolution speed of 20 r/s. Fig. 2a describes the pressure distribution on the suspended cylindrical surface near the blade root. When the fluid flowed through the blade rapidly, the pressure difference phenomenon and accompanying flow separation occurred on the nose. All three turbulence models were able to capture these transient flow characteristics well. Fig. 2b shows the coherent structures behind the propeller at Q-criterion=0.015. In general, the three models provided very similar instantaneous structures downstream of the blade tip. But for the root-vortex, DLES obtained chaotic and intense vortex structures, DDES obtained relatively small and simple structures, and SBES obtained relatively orderly structures.

For comparison, detailed velocity measurements behind the propeller are available (Chesnakas and Jessup, 1998) for a mid-plane at a downstream location x/R=0.2386, where x is the axial distance and R is the propeller radius. Fig. 3 depicts the contours of circumferential average velocity components in the axial, tangential, and radial directions. The simulation and experimental results were plotted in the dimensionless radial coordinates (r/R), where r is the radial distance to the centerline. The numerical results showed a good agreement with the experimental results in terms of the axial velocity (V_a) and

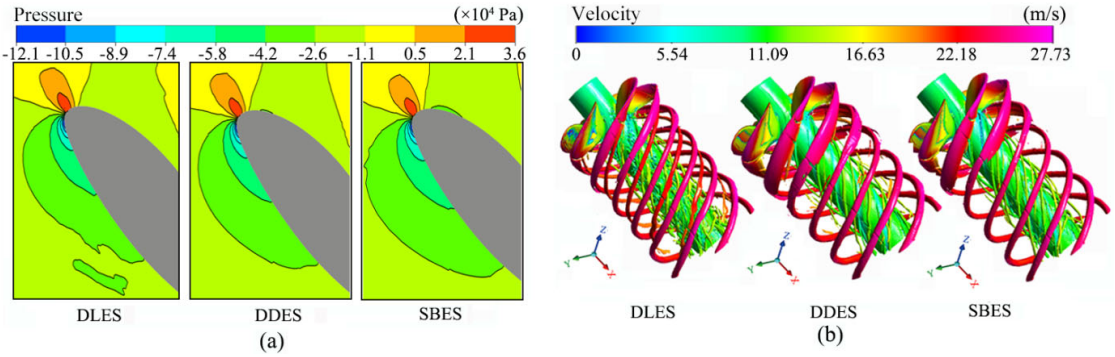

Fig. 2 Numerical predictions of the flow field
(a) Pressure distribution near the blade root; (b) Vortex distribution behind the propeller

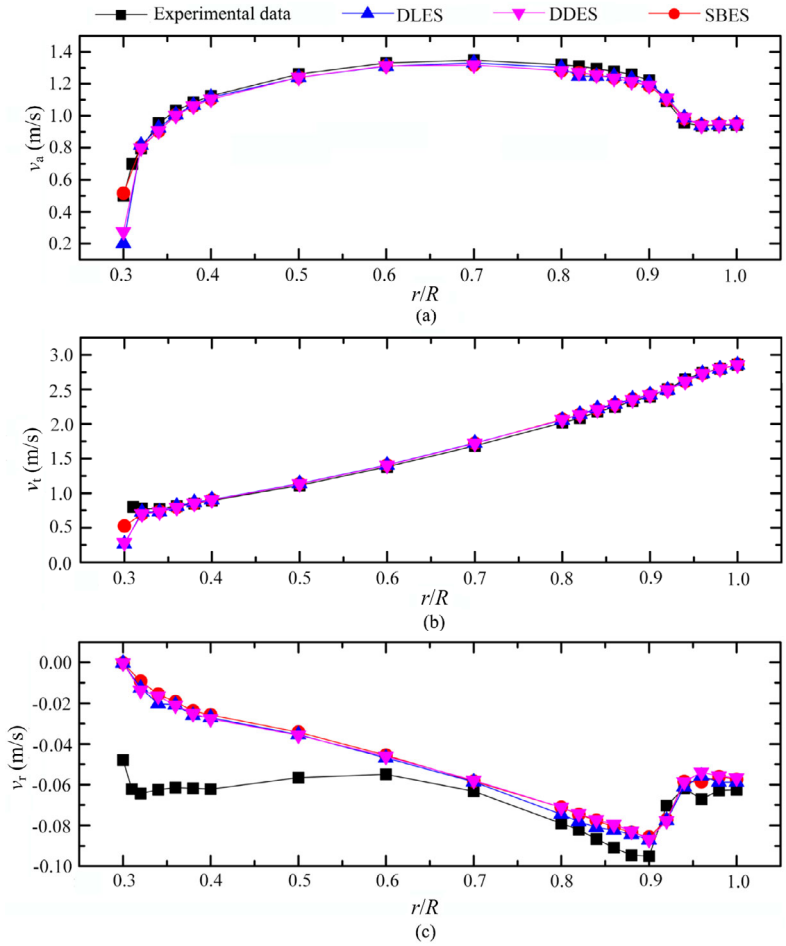

Fig. 3 Variation of three velocity components in the plane of x/R=0.2386: axial (a), tangential (b), and radial (c) directions

tangential velocity (V_t). However, the agreement for radial velocity (V_r) in the region near the hub (where r/R is smaller) was not as good. We suspect that this difference was due to the relatively long hub, resulting in unsatisfactory development of the boundary layer near the hub and insufficient regional grid resolution in the area. However, its values were an order of magnitude smaller than V_a and V_t. On the whole, all turbulence models returned similar results consistent with the experimental data, which illustrates the accuracy of the SRS method in performance prediction.

4 PIV system of the scaled propeller

4.1 Experimental setup

To obtain insights into the real-time wake flow of the propeller, a 2D-PIV test bench was established to investigate the transient flow information. Fig. 4 shows an overall view of the experimental setup. The basic layout comprised a laser, a charged couple device (CCD) camera, a transparent water tank, a propeller model, a geared motor, and a water pump. The results related to a fixed frame *O*-*XYZ*, with the origin *O* set at the geometric center of the propeller, the *X* axis along the shaft centerline outward, the *Y* axis along the horizontal, the *Z* axis along the upward vertical, and the *XY* plane at the propeller itself. Laser light was provided by a Nano TRL laser with 400 mJ energy per pulse, which illuminated the visual field through laser optics and formed a laser sheet of 1 mm thickness and 15° field angle. A LaVision Imager LX camera (1600×1200 pixels, 14 bit resolution, 7.4 μm pixel pitch) and a Nikon AF lens (50 mm f/1.8) was used to acquire raw images. Post-processing was performed with LaVision Davis 8.0 software. One hundred sets of images were recorded at a maximum acquisition frequency of 2 Hz. The camera and laser were combined with the computer via a timing controller to control the timing required to capture images and laser illumination.

In the low-speed flow field, the rotating speeds were defined as 80 r/min and 300 r/min, respectively. When the density of tracer particles was close to the water density (i.e. had a specific gravity of about 1), their movement trajectories could reflect the actual water flow. Therefore, polystyrene microspheres with a density of 1.06 g/cm^3 and an average diameter of 10 μm were selected as the tracer particles. A mixture of 1 g of polystyrene microspheres and 40 L of water was put into the water tank.

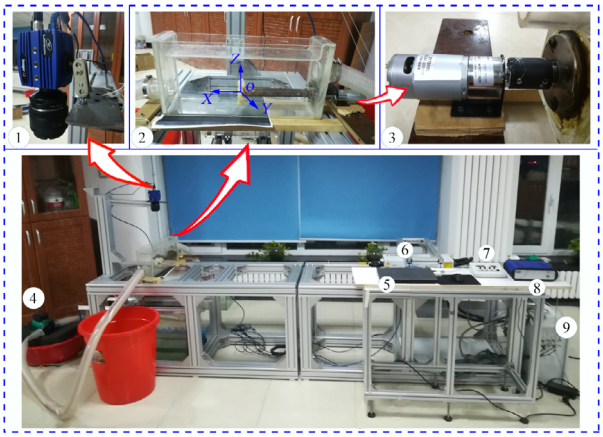

Fig. 4 Basic layout of the PIV system
1: CCD camera; 2: water tank system; 3: driving system; 4: water pump; 5: computer; 6: laser; 7: control panel; 8: timing controller; 9: power supply

4.2 Calibration

Particle trajectories were displayed as pixels in the image. To obtain the corresponding relationship between pixel and millimeter, the CCD camera was calibrated to determine actual displacement of the particle. A transparent calibration scale was first placed in the measurement plane (Fig. 5). After taking the current image, the calibration procedure was completed by selecting any points *a* and *b* on the calibration scale and inputting the actual size under the calibration function of the LaVision Davis software. When carrying out test data acquisition, the rotation rate of the working motor was measured by the photoelectric speedometer. The time interval for each shot was determined until the same particle in two adjacent images moved between 5 and 15 pixels. Then the data collection was performed and 100 photos were taken at each rotation rate.

4.3 Extraction of flow information

The flow information was extracted from a rectangular area behind the propeller, located on a horizontal plane passing through the axis of the propeller and 29 mm from the propeller center (Fig. 6a). Due to the limitations of the shooting size during the experiment, the size of the square region of the flow field was 0.1 m×0.1 m.

To perform quantitative analysis of the velocity, the velocity values on a straight line perpendicular to the center line in the rectangle were extracted. The straight line was 29 mm from the center of the propeller (coordinates x=29 mm, z=0 mm). In addition, a square mask (Fig. 6b) was added to the image taken by the PIV for flow field capture. Preliminary observation of the PIV velocity field in the mask could be carried out after image post-processing (Fig. 6c).

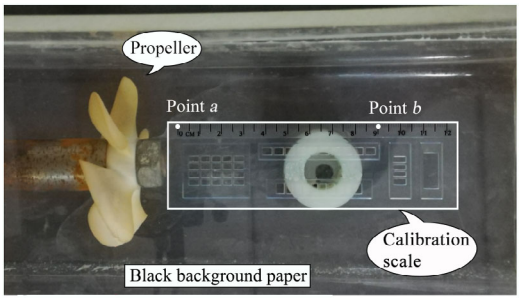

Fig. 5 PIV size calibration

5 Numerical simulation of the scaled-down propeller flow

5.1 Mesh layout and simulation details

For comparison with the experiment, a cuboid was adopted as the external flow field in the simulation model, and the interfaces between the actual water pipe and the water tank were replaced by the boundary inlet and outlet. The rotation domain consisted of a 0.2 times proportional propeller with a diameter of 80.54 mm. The overall grid layout is shown in Fig. 7a. The meshes of the inlet cross section and the blade surface are shown in Figs. 7b and 7c, respectively. The total mesh number was 7.890 million, of which the rotating domain and the fixed domain accounted for 6.814 million and 1.076 million, respectively. In addition, the mesh quality of the whole computational domain was greater than 0.4 (Fig. 7d). To obtain a sufficient range of vortices, the numbers of time steps were 1500 and 800 at low and

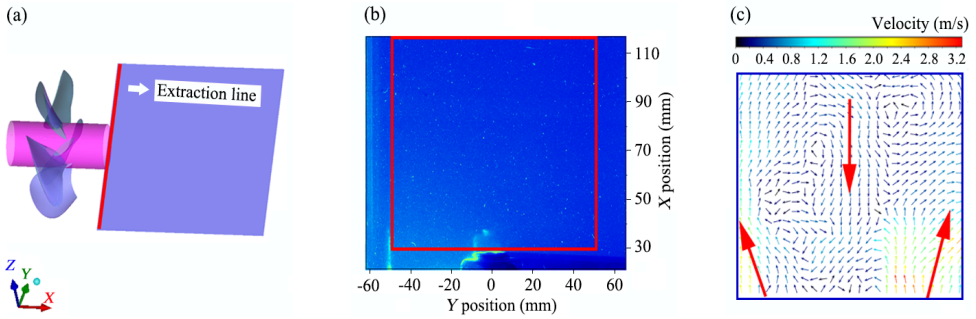

Fig. 6 Extraction of flow field results

(a) Rectangular flow field and velocity value extraction line; (b) Example of a collected image; (c) Post-processing results

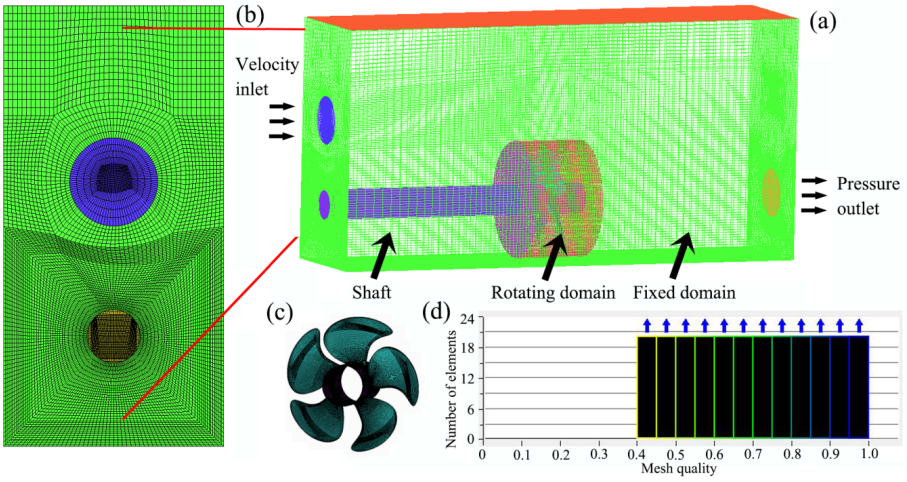

Fig. 7 Numerical simulation model of the scaled-down propeller

(a) Computational domain; (b) Local mesh section; (c) Blade surface mesh; (d) Mesh quality

high rotating speeds, respectively. Other simulation details were the same as those used for the numerical method of the entire propeller.

5.2 Average velocity analysis of the straight line

The evolution of the 3D flow field around the propeller was related to its blade position, which determined the instantaneous velocity fluctuation downstream. A quantitative study of velocity variation was carried out by extraction of the average velocity on the straight line (x=0.029 m, z=0 m) (Fig. 8). Numerical data from the CFD simulation plotted in the right frame were used for comparison with the experimental data. Variation in the relative positions of the propeller blade and the measuring plane caused fluctuation of the average velocity. Therefore, in the results from 10 tests, the average speed varied within a certain range due to the difference in the initial position of the propeller. However, the average velocity was of the same order of magnitude, which meant that the wake flow was well developed. The significance of the average velocity fluctuation range was that the average velocity measured in any experiment had the highest probability of falling within this range, i.e. it could be considered to change within this range. Since the initial position of the blade in CFD calculation was fixed, the numerical result was not compared with a specific experiment. However, the predicted values of the three models were all within the fluctuation range, which verified the correctness and feasibility of the numerical simulation method.

5.3 Comparison of measured and calculated wake field results

Instantaneous velocity and vorticity distributions in the square area obtained by PIV measurements and CFD simulations are compared in Figs. 9 and 10. The curvature of streamlines reflects the intensity of velocity variation, so a vortex is usually formed at a large curvature. Fig. 9a shows that the high-speed region was concentrated mainly near the blades at a speed of 80 r/min. However, the contours of DLES and DDES showed that the high-speed region was far away from the propeller. They also showed that a larger semi-annular vortex formed at the top of the image. The velocity profiles calculated by the three models all exhibited this characteristic. But for the vortex behind the blades, locations predicted by DLES and DDES deviated to the shaft rear and the tank wall.

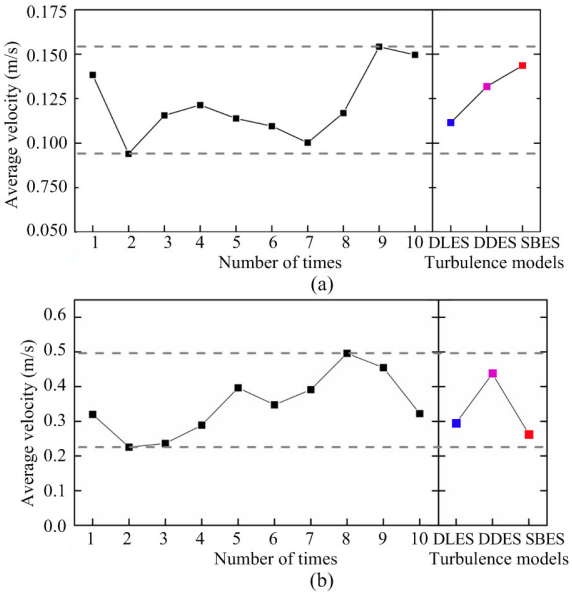

Fig. 8 Average velocity of the straight line
(a) Rotating speed=80 r/min; (b) Rotating speed=300 r/min

When the rotating speed reached 300 r/min, the high-speed region stretched outward mainly along the tank body (Fig. 9b). The streamline indicated that a vortex appeared far away from the propeller. It was obvious that DDES and DLES showed unreasonable predictions on the right side of the contour. Also, the flow field predicted by DLES was too scattered and there was no continuity in velocity values compared with those of the other two methods. It was clear that DLES had more unreasonable vortices near the blades. Overall, the velocity and vortex distributions were well analyzed by SBES.

Fig. 10 depicts the instantaneous vorticity characteristics of the flow field behind the propeller. The positive and negative values of the PIV experiment actually represented the rotation direction of the vortex, which could be judged according to the right-hand rule. More notably, all three models predicted high vorticity values close to the water tank, but this feature was not evident from the experimental results. This was because the SRS models were relatively sensitive to capturing the small vortices, while the resolution of the PIV experiment to small vortices was weak.

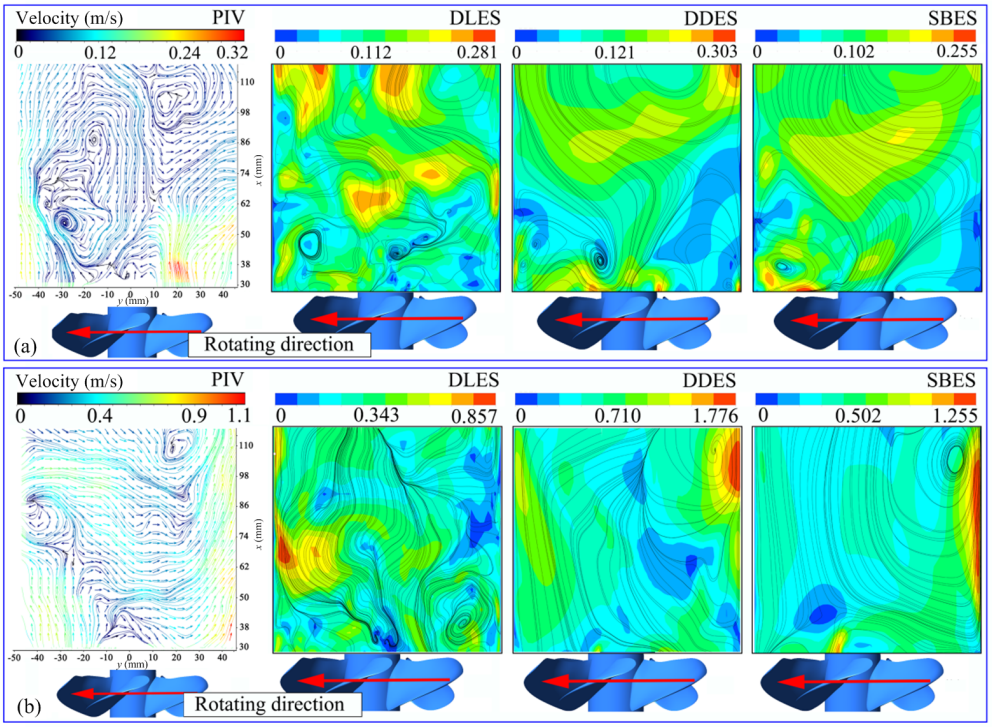

Fig. 9 Instantaneous velocity field distribution
(a) Rotating speed=80 r/min; (b) Rotating speed=300 r/min

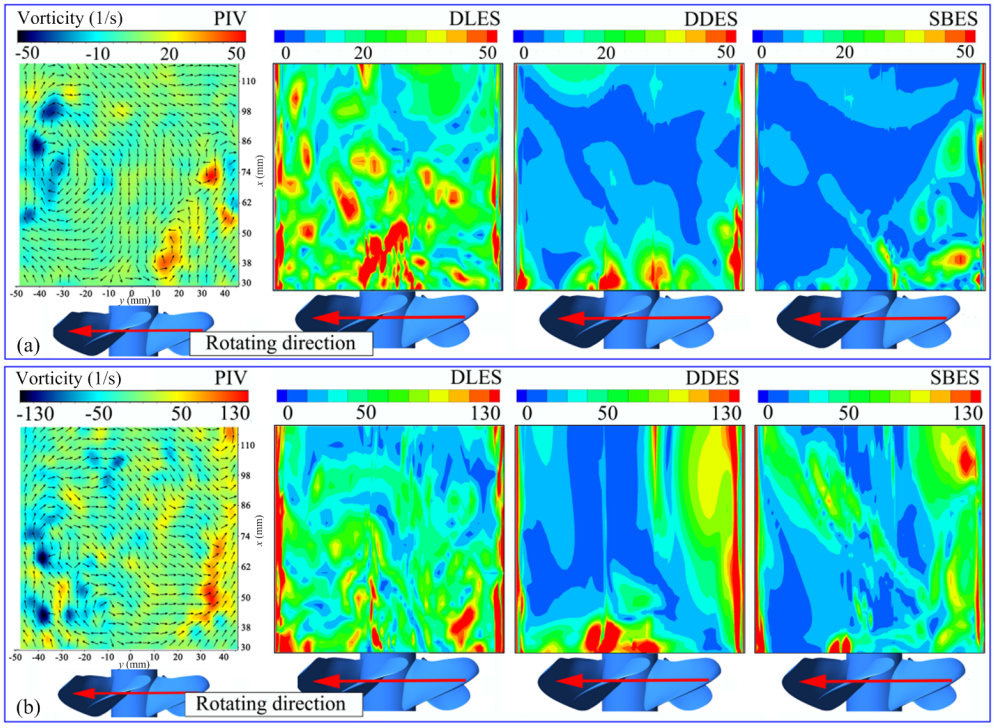

Fig. 10 Instantaneous vorticity distribution
(a) Rotating speed=80 r/min; (b) Rotating speed=300 r/min

In Fig. 10a, the high and low vorticity regions are located mainly in the lower right and middle left of the test image, respectively. In the whole flow field, a wide range of high vorticity distribution was obtained by DLES, in contrast to the results from PIV analysis. DDES had unreasonable vorticity regions behind the propeller shaft. A similar phenomenon can also be seen in Fig. 10b in which the positions of high vorticity obtained by DLES and DDES are not consistent with the measurement results. From the minimum numbers of vortices obtained by DDES, it seems that the turbulence captured by this model had not been fully developed. In contrast, the results of SBES were closely aligned with the PIV measurements, which showed high vorticity generated on the right side flow field and behind the blades.

6 Conclusions

In this study, the wake evolution characteristics of a P5168 propeller were investigated by combining numerical simulation with flow measurement. CFD based on the SRS method was used for numerical simulation, and the PIV system was used for flow field measurement. The numerical simulation details, test bench, and operation process were described, and the results of velocity distribution and vorticity distribution analyzed. The test results were in accordance with the basic flow field characteristics, and the validity of the numerical simulation was comprehensively evaluated through comparison with PIV results. The conclusions can be summarized as follows:

1. In the full-scale propeller model, DLES, SBES, and DDES predicted quite similar flow separation behaviors and associated tip vortex structures over the blade. However, for the wake vortices at the blade root, DLES predicted strongly disordered vortex structures, while the transient turbulence results observed with SBES were relatively orderly.

2. At a design advance ratio of J=1.1, predicted velocity components at a downstream plane showed a very similar pattern and good agreement with reference test data. The PIV test results showed the velocity and vorticity distribution of the flow field, which can represent the actual flow situation to a considerable extent.

3. In the SRS method, DLES generated a large number of vortex structures, but the vortex distribution was too dispersed with larger numerical values, which was inconsistent with the characteristics of experimental performance. Because of insufficient development of vortex structures, the ability of DDES to capture flow field information was unsatisfactory. By comparison, the velocity distribution and vorticity distribution predicted by SBES were in good agreement with experimental results, reflecting its effectiveness and advancement.

Contributors

Chun-bao LIU wrote the first draft of the manuscript. Jing LI revised and edited the final version. Tong-jian WANG managed the execution of research activity. Yuan LI assisted in the experiments.

Conflict of interest

Chun-bao LIU, Jing LI, Yuan LI, and Tong-jian WANG declare that they have no conflict of interest.

References

Chase N, Carrica PM, 2013. Submarine propeller computations and application to self-propulsion of DARPA Suboff. *Ocean Engineering*, 60:68-80. https://doi.org/10.1016/j.oceaneng.2012.12.029

Chesnakas C, Jessup S, 1998. Experimental characterization of propeller tip flow. Proceedings of the 22nd Symposium on Naval Hydrodynamics, p.156-169.

Dubbioso G, Muscari R, Ortolani F, et al., 2017. Analysis of propeller bearing loads by CFD. Part I: straight ahead and steady turning maneuvers. *Ocean Engineering*, 130:241-259. https://doi.org/10.1016/j.oceaneng.2016.12.004

Felli M, Falchi M, Dubbioso G, 2015. Hydrodynamic and hydroacoustic analysis of a marine propeller wake by TOMO-PIV. Proceedings of the 4th International Symposium on Marine Propulsors.

Gritskevich MS, Garbaruk AV, Schütze J, et al., 2012. Development of DDES and IDDES formulations for the *k-ω* shear stress transport model. *Flow, Turbulence and Combustion*, 88(3):431-449. https://doi.org/10.1007/s10494-011-9378-4

Jahoda M, Moštěk M, Kukuková A, et al., 2007. CFD modelling of liquid homogenization in stirred tanks with one and two impellers using large eddy simulation. *Chemical Engineering Research and Design*, 85(5):616-625. https://doi.org/10.1205/cherd06183

Kleinwächter A, Ebert E, Kostbade R, et al., 2015. PIV as a novel full-scale measurement technique in cavitation research. Proceedings of the 3rd International Symposium on Marine Propulsors.

Kleinwächter A, Hellwig-Rieck K, Heinke HJ, et al., 2017. Full-scale total wake field PIV-measurements in comparison with ANSYS CFD calculations: a contribution to a better propeller design process. *Journal of Marine Science and Technology*, 22(2):388-400. https://doi.org/10.1007/s00773-016-0418-6

Korsström A, Miettinen P, Hänninen SK, et al., 2015.

Investigation of the propeller slip stream over an Azipod propulsor by PIV measurements and CFD simulations. Proceedings of the 4th International Symposium on Marine Propulsors.

Kumar P, Mahesh K, 2015. Analysis of marine propulsor in crashback using large eddy simulation. Proceedings of the 4th International Symposium on Marine Propulsors.

Kumar P, Mahesh K, 2016. Towards large eddy simulation of hull-attached propeller in crashback. Proceedings of the 31st Symposium on Naval Hydrodynamics.

Kumar P, Mahesh K, 2017. Large eddy simulation of propeller wake instabilities. *Journal of Fluid Mechanics*, 814:361-396. https://doi.org/10.1017/jfm.2017.20

Li ZP, Song G, Bao YY, et al., 2013. Stereo-PIV experiments and large eddy simulations of flow fields in stirred tanks with Rushton and curved-Blade turbines. *AIChE Journal*, 59(10):3986-4003. https://doi.org/10.1002/aic.14117

Lin D, Su XR, Yuan X, 2018. DDES analysis of the wake vortex related unsteadiness and losses in the environment of a high-pressure turbine stage. *Journal of Turbomachinery*, 140(4):041001. https://doi.org/10.1115/1.4038736

Liu CB, Li J, Bu WY, et al., 2018. Application of scale-resolving simulation to a hydraulic coupling, a hydraulic retarder, and a hydraulic torque converter. *Journal of Zhejiang University-SCIENCE A* (*Applied Physics and Engineering*), 19(12):904-925. https://doi.org/10.1631/jzus.A1700508

Menter FR, 2012. Best Practice: Scale-resolving Simulations in ANSYS CFD. ANSYS Germany GmbH.

Mizzi K, Demirel YK, Banks C, et al., 2017. Design optimisation of Propeller Boss Cap Fins for enhanced propeller performance. *Applied Ocean Research*, 62:210-222. https://doi.org/10.1016/j.apor.2016.12.006

Mofidi A, Carrica PM, 2014. Simulations of zigzag maneuvers for a container ship with direct moving rudder and propeller. *Computers & Fluids*, 96:191-203. https://doi.org/10.1016/j.compfluid.2014.03.017

Morgut M, Nobile E, 2012. Influence of grid type and turbulence model on the numerical prediction of the flow around marine propellers working in uniform inflow. *Ocean Engineering*, 42:26-34. https://doi.org/10.1016/j.oceaneng.2012.01.012

Ning Z, Hu H, 2016. An experimental study on the aerodynamics and aeroacoustic characteristics of small propellers. Proceedings of the 54th AIAA Aerospace Sciences Meeting, p.1785. https://doi.org/10.2514/6.2016-1785

Ning Z, Wlezien RW, Hu H, 2017. An experimental study on small UAV propellers with serrated trailing edges. Proceedings of the 47th AIAA Fluid Dynamics Conference, p.3813. https://doi.org/10.2514/6.2017-3813

Paik KJ, Hwang S, Jung J, et al., 2015. Investigation on the wake evolution of contra-rotating propeller using RANS computation and SPIV measurement. *International Journal of Naval Architecture and Ocean Engineering*, 7(3):595-609. https://doi.org/10.1515/ijnaoe-2015-0042

Seo J, Seol DM, Han B, et al., 2016. Turbulent wake field reconstruction of VLCC models using two-dimensional towed underwater PIV measurements. *Ocean Engineering*, 118:28-40. https://doi.org/10.1016/j.oceaneng.2016.03.021

Yang Y, Zhou T, Sciacchitano A, et al., 2017. Experimental investigation of the impact of a propeller on a streamwise impinging vortex. *Aerospace Science and Technology*, 69:582-594. https://doi.org/10.1016/j.ast.2017.07.017

Yang Y, Sciacchitano A, Veldhuis LLM, et al., 2018. Analysis of propeller-induced ground vortices by particle image velocimetry. *Journal of Visualization*, 21(1):39-55. https://doi.org/10.1007/s12650-017-0439-1

Yang ZY, 2015. Large-eddy simulation: past, present and the future. *Chinese Journal of Aeronautics*, 28(1):11-24. https://doi.org/10.1016/j.cja.2014.12.007

Yao JX, 2015. Investigation on hydrodynamic performance of a marine propeller in oblique flow by RANS computations. *International Journal of Naval Architecture and Ocean Engineering*, 7(1):56-69. https://doi.org/10.1515/ijnaoe-2015-0005

中文概要

题　目：船用螺旋桨流动尺度解析模拟与粒子图像测速验证

目　的：船用螺旋桨性能评估中常用的雷诺平均方法（RANS）存在许多难题，特别是在处理边界层发展、尺度效应、翼尖和轮毂涡等复杂流动现象时。本文使用动态大涡模拟（DLES）、延迟分离涡模拟（DDES）和应力混合涡模拟（SBES）三种尺度解析模拟（SRS）方法，以提高流动特性预测的准确性。

创新点：1. 通过 SRS 方法详细地描述螺旋桨流场的不规则和多尺度湍流结构；2. 通过粒子图像测速（PIV）试验，分析缩比螺旋桨的真实流场。

方　法：1. 考虑叶片的周期分布和计算消耗，提取 1/5 的螺旋桨计算区域，并采用局部网格细化方法，获得分辨率足够高的网格模型（图 1）；通过仿真结果与已有试验数据的对比，验证 SRS 方法在螺旋桨性能预测方面的可行性与有效性（图 3）。2. 通过搭建 PIV 试验装置（图 4），得到缩比螺旋桨在特定横截面上的速度和涡量分布情况下的尾流演变（图 9 和 10），从而分析 SRS 方法对流场结构的捕捉能力。

结　论：1. 通过定量和定性分析发现，SRS 方法在预测特征参数和捕捉流场信息方面表现良好，特别是值得重点关注的 SBES 模型；2.作为一种可视化流场分析工具，PIV 测量方法可以为螺旋桨等旋转机械的设计和性能改进提供一定的参考依据。

关键词：螺旋桨；数值模拟；尺度分辨模拟；PIV 试验